JOURNAL OF GEOPHYSICAL RESEARCH: ATMOSPHERES, VOL. 118, 12,948–12,961, doi:10.1002/2013JD020632, 2013

Estimating aerodynamic roughness over complex surface terrain

Joanna M. Nield,[1] James King,[2] Giles F. S. Wiggs,[2] Julian Leyland,[1] Robert G. Bryant,[3] Richard C. Chiverrell,[4] Stephen E. Darby,[1] Frank D. Eckardt,[5] David S. G. Thomas,[2,5,6] Larisa H. Vircavs,[1] and Richard Washington[2]

Received 26 July 2013; revised 7 November 2013; accepted 11 November 2013; published 9 December 2013.

[1] Surface roughness plays a key role in determining aerodynamic roughness length (z_o) and shear velocity, both of which are fundamental for determining wind erosion threshold and potential. While z_o can be quantified from wind measurements, large proportions of wind erosion prone surfaces remain too remote for this to be a viable approach. Alternative approaches therefore seek to relate z_o to morphological roughness metrics. However, dust-emitting landscapes typically consist of complex small-scale surface roughness patterns and few metrics exist for these surfaces which can be used to predict z_o for modeling wind erosion potential. In this study terrestrial laser scanning was used to characterize the roughness of typical dust-emitting surfaces (playa and sandar) where element protrusion heights ranged from 1 to 199 mm, over which vertical wind velocity profiles were collected to enable estimation of z_o. Our data suggest that, although a reasonable relationship ($R^2 > 0.79$) is apparent between 3-D roughness density and z_o, the spacing of morphological elements is far less powerful in explaining variations in z_o than metrics based on surface roughness height ($R^2 > 0.92$). This finding is in juxtaposition to wind erosion models that assume the spacing of larger-scale isolated roughness elements is most important in determining z_o. Rather, our data show that any metric based on element protrusion height has a higher likelihood of successfully predicting z_o. This finding has important implications for the development of wind erosion and dust emission models that seek to predict the efficiency of aeolian processes in remote terrestrial and planetary environments.

Citation: Nield, J. M., et al. (2014), Estimating aerodynamic roughness over complex surface terrain, *J. Geophys. Res. Atmos.*, *118*, 12,948–12,961, doi:10.1002/2013JD020632.

1. Introduction

[2] The ability to quantify the momentum transfer between fluid flow and small-scale roughness elements is important in a myriad of environmental contexts including wind erosion and sediment entrainment schemes [e.g. *Lettau*, 1969; *MacKinnon et al.*, 2004; *Lancaster*, 2004; *Lancaster et al.*, 2010], energy balance modeling [e.g. *Brock et al.*, 2006; *Manes et al.*, 2008], and urban heat exchange [*Oke*, 1987]. This momentum transfer is parameterized by aerodynamic roughness, z_o, and is a function of surface roughness, k, and the arrangement and size of roughness elements [*Raupach et al.*, 1991]. While vertical wind velocity profile or shear stress measurements can be used to measure z_o directly [*King et al.*, 2008], there are many instances where only measurements of surface roughness (k) are available [*Greeley et al.*, 1997]. Relationships between k to z_o are therefore required [*MacKinnon et al.*, 2004], particularly for small-scale (sub-cm) roughness patterns, which to date have been little studied [*Manes et al.*, 2008] and present additional challenges due to their continuous and complex morphologies [*Marticorena et al.*, 2006]. Aerodynamic roughness over larger patterns is generally parameterized through investigations of discrete roughness elements at a wide range of spatial scales from small-scale wind tunnel studies [*Brown et al.*, 2008; *Cheng et al.*, 2007; *King et al.*, 2008], medium-scale vegetation, and nebkha dune elements [*Gillies et al.*, 2007; *King et al.*, 2006; *Lancaster and Baas*, 1998; *Marticorena and Bergametti*, 1995; *Raupach*, 1992; *Raupach et al.*, 1993; *Wolfe and Nickling*, 1993] to large-scale building roughness elements of major cities [*Castro et al.*, 2006; *Grimmond and Oke*, 1999; *Millward-Hopkins et al.*, 2011; *Rotach*, 1995; *Zaki et al.*, 2011] and remote sensing investigations [*Blumberg and Greeley*, 1993; *Laurent*

The copyright line for this article was changed on 23 OCT 2014 after original online publication.

[1]Geography and Environment, University of Southampton, Southampton, UK.
[2]School of Geography and the Environment, Oxford University Centre for the Environment, University of Oxford, Oxford, UK.
[3]Department of Geography, University of Sheffield, Sheffield, UK.
[4]School of Environmental Sciences, University of Liverpool, Liverpool, UK.
[5]Department of Environmental and Geographical Science, University of Cape Town, Cape Town, South Africa.
[6]School of Geography, Archaeology and Environmental Studies, University of the Witwatersrand, Johannesburg, South Africa.

Corresponding author: J. M. Nield, Geography and Environment, University of Southampton, Highfield, Southampton, SO17 1BJ, UK. (J.Nield@soton.ac.uk)

2169-897X/13/10.1002/2013JD020632

et al., 2005; *Prigent et al.*, 2005]. In wind tunnel studies that assessed element configuration *Cheng et al.* [2007] and *Brown et al.* [2008] found that the roughness element density, rather than configuration, had the greatest influence on shear stress partitioning. Most aeolian transport field studies only consider discrete roughness elements such as vegetation, but the performance of sediment entrainment schemes for surfaces with continuous microroughness is less well quantified [*MacKinnon et al.*, 2004] or parameterized using grain size [*Darmenova et al.*, 2009]. Playas (or salt pans [*Shaw and Bryant*, 2011]) and small-scale rocky terrain surfaces (e.g., desert stony surfaces [*Bullard et al.*, 2011] and sandar [*Prospero et al.*, 2012]) typically comprise crusts or rock patterns of connected roughness elements at different scales. Although these elements are shorter than more commonly studied vegetation elements [e.g., *Eamer and Walker*, 2010; *Brown and Hugenholtz*, 2011; *Weligepolage et al.*, 2012; *Paul-Limoges et al.*, 2013], they still have the potential to significantly alter z_o and the threshold wind stress for sediment transport [*Wiggs and Holmes*, 2011]. These complex, rough, continuous surfaces present additional challenges for measurement and turbulence characterization, such that field studies to date have generally only undertaken transect measurements to characterize their roughness [e.g., *Lettau*, 1969; *Lyles and Allison*, 1979; *Greeley et al.*, 1995; *Lancaster*, 2004; *Brock et al.*, 2006]. However, with the development of new technologies such as terrestrial laser scanning (TLS), the opportunity now exists to characterize surface roughness metrics in high resolution (mm scale) and in 3-D. These data sets can provide vital estimations of z_o in areas where measuring aerodynamic profiles are infeasible but shear stress and erosion potential calculations are essential.

[3] TLS is a technique whereby spatial coordinates of a surface are measured remotely in a short time (minutes) over a moderate area (tens of square meters), thus enabling quantification of surface roughness at sub-cm scale [*Buckley et al.*, 2008]. TLS has been used in a range of environments to specifically measure small-scale surface roughness including (i) sand and soils [*Eitel et al.*, 2011; *Haubrock et al.*, 2009; *Nield et al.*, 2011; *Nield and Wiggs*, 2011; *Rodriguez-Caballero et al.*, 2012; *Sankey et al.*, 2010; *Smith et al.*, 2011], (ii) vegetation [*Anderson et al.*, 2010; *Antonarakis et al.*, 2009; *Weligepolage et al.*, 2012], (iii) snow and ice [*Kaasalainen et al.*, 2011; *Nield et al.*, 2013; *Wirz et al.*, 2011], and (iv) rocks [*Fardin et al.*, 2004; *Khoshelham et al.*, 2011] and has shown promise in relating these patterns to aerodynamic roughness [*Hugenholtz et al.*, 2013]. Here we apply TLS to elucidate pattern variability over a broad range of roughness element sizes and pattern distributions associated with 20 typical playa and sandar dust-emitting surfaces [*Mahowald et al.*, 2003; *Prospero et al.*, 2012]. We relate the quantified morphological characteristics (flat to cobble) to velocity profile-determined aerodynamic roughness (z_o) values and provide a continuum of predictive measurements for relatively smooth, complex patterns that are typically prone to wind erosion.

2. Background: Quantifying Surface Roughness

[4] The availability of accurate, high-resolution DEMs derived from TLS surveys opens up the possibility of using a myriad of different terrain analysis techniques to quantify surface roughness magnitude and variation in one, two, or three dimensions. Conceptually, these different methodologies define the magnitude of the surface elements' height and spacing, or the variability of the surface patterning, as indicated in Table 1.

2.1. One-Dimensional Methods

[5] The simplest methods for characterizing surfaces consider the height distribution of the surface, where the maximum and standard deviation of height are taken to indicate element magnitude and roughness (surface variability), respectively [*Glenn et al.*, 2006]. These nonspatially explicit metrics are commonly used as a measure of surface roughness in the analysis of complex large-scale building cityscapes or forested terrain [*Nakayama et al.*, 2011].

2.2. Two-Dimensional Methods

[6] Two-dimensional (2-D) methods that characterize the spatial aspects of surface roughness have traditionally been undertaken using transects of varying length. For example, in glacial research *Munro* [1989] adapted the *Lettau* [1969] method (LM) to characterize complex ice roughness. This LM method is calculated using equations (1–3) from *Munro* [1989] and has been compared to aerodynamic measurements made by a number of researchers (e.g., *Brock et al.* [2006]). In the LM method transect lines are detrended and centered over a zero mean. The zero-up-crossing method [*Goda*, 2000] can then be used to calculate how many times the zero line is crossed in an upward direction through the transect line to give the frequency of continuous groups of positive height deviations:

$$k_{\mathrm{LM}} = 0.5h^{*}\left(\frac{s}{S}\right) \tag{1}$$

$$s = \frac{h^{*}X}{2f} \tag{2}$$

$$S = \left(\frac{X}{f}\right)^{2} \tag{3}$$

where k_{LM} is the geometric roughness length equivalent of measured aerodynamic roughness using the LM method, h^* is the average obstacle height (twice the standard deviation of the detrended elevation in equation (2)), s is the silhouette area, S is the unit ground area, X is the length of the transect, and f is the roughness element frequency (number of continuous groups of positive height deviations above the mean elevation—calculated using the zero-up-crossing method in this instance).

[7] The zero-up-crossing method enables wavelength and heights for each element to be calculated along a transect. The converse zero-down-crossing method can be used to determine when the zero line is crossed in a downward direction, and the difference between neighboring up and down crossing pairs determines the ridge width and the distance between down and up pairs defines the interridge spacing (S_p). While discrete elements are generally assumed to be cylindrical for roughness density calculations [*MacKinnon et al.*, 2004; *Raupach et al.*, 1993], complex surfaces can be simplified as intersecting patterns where one unit ends when it joins a perpendicular element. Roughness density

Table 1. Classification of Different Physical Surface Roughness Metrics in Terms of Pattern Variability, Shape, and Magnitude

Analysis dimension	Metric			Surface Roughness Characterization: Magnitude: Vertical	Horizontal	Variability	Shape
1-D	Standard deviation of elevation distribution					x	
2-D	Zero-up-crossing transects		Height (mean)	x			
			Height (max)	x			
			Height (standard deviation)			x	
			Ridge width		x		
			Ridge wavelength		x		
			Interridge spacing		x		
			R_{BF}				x
			$\lambda_{2\text{-D}}$				x
			k_{LM}				x
	Semivariogram		Sill	x			
			Range			x	
3-D	Moving window analysis	Mean of elevation standard deviations	Interface width	x			
			Saturation length			x	
		Standard deviation of elevation standard deviations	Peak value			x	
			Range			x	
		Root-mean-squared height (RMSH)	Interface width	x			
			Saturation length			x	
		Maximum height	Interface width	x			
			Saturation length			x	
	Fourier transform		magnitude relative to flat surface		x		
			dominant wavelength		x		
	Wavelet		magnitude relative to flat surface		x		
			dominant wavelength		x		
	R_{SA}						x
	λ_{vol}						x

($\lambda_{2\text{-D}}$) can then be specified from equation (4), assuming a rectangular element cross section.

$$\lambda_{2\text{-D}} = \frac{b_1 h_1}{L_2 L_1} \quad (4)$$

where b_1 is the element width perpendicular to the wind direction, h_1 is the element height, L_1 is the element wavelength perpendicular to the wind direction, and L_2 is the element wavelength parallel to the wind direction.

[8] Similarly, a basal to frontal area ratio (R_{BF}) can be calculated using equation (5).

$$R_{BF} = \frac{L_2 b_1}{h_1 b_1} \quad (5)$$

[9] Variograms are used in a range of continuous surface roughness studies to assess pattern scaling, including in gravel river beds [*Hodge et al.*, 2009; *Huang and Wang*, 2012], soil [*Croft et al.*, 2012, 2013; *Sankey et al.*, 2012], and snow surfaces [*Schirmer and Lehning*, 2011]. Commonly derived values include the sill, which is the value of semi-variance (y) at which convergence occurs and indicates roughness within the data, and the range, which is the corresponding lag distance (x) at convergence and indicates the point at which surface structures are no longer related.

2.3. Three-Dimensional Methods

[10] Three-dimensional (3-D) methods capture the full spatial variability of the surface either locally via moving windows, or globally via complete surface analysis. Similar to the 2-D method, the standard deviation of elevations can be measured spatially by quantifying the convergent standard deviation value within moving windows of increasing size [*Frankel and Dolan*, 2007], as has been used in a variety of applications including biological crust roughness [*Rodriguez-Caballero et al.*, 2012].

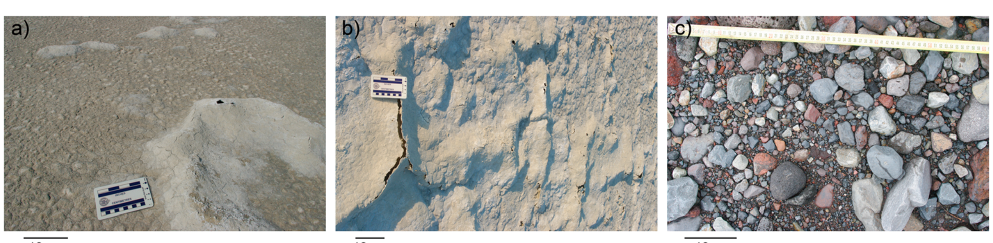

Figure 1. Examples of (a) irregular salt pan, (b) regular, polygonal salt pan, and (c) sandur surface patterns measured using the TLS.

Table 2. Surface Description for Each Site[a]

Site Name	Surface Type	Pattern Description
A1/H1	salt pan	polygonal ridges
A2/H1	salt pan	polygonal ridges
A3/H1	salt pan	polygonal ridges
A4/H2	salt pan	mixed continuous with domed ridges
A5/H2	salt pan	mixed polygonal ridges and degraded surfaces
A6/H1	salt pan	mixed domed ridges and degraded surfaces
A7/H2	salt pan	degraded surface
A8/H4	salt pan	continuous surface with microdomes
A9/H2	salt pan	polygonal ridges
A10/H4	salt pan	flat, continuous surface
A11/H2	salt pan	low polygonal ridges
A12/H2	salt pan	mixed degraded with occasional ridges
B1/H1	salt pan	polygonal ridges
B2/H1	salt pan	mixed polygonal ridges and degraded surfaces
B3/H3	sandur	stabilized terrace with rounded volcanic fluvial sediments
B4/H6	sandur	active braided river with volcanic fluvial sediments
C1/H5	salt pan	polygonal ridges
C2/H1	salt pan	polygonal ridges
D1/H2	salt pan	mixed continuous with occasional polygonal ridges
D2/H2	salt pan	mixed continuous with occasional domed ridges

[a]Site names are based on cluster analysis (Figures 4 and 5). Refer to Figures 1 and 6 for photos and TLS planform DEMs of each site.

Taking the average of any descriptive statistic at each moving window size enables us to specify an interface width (the maximum roughness value) and saturation length (window size at which values converge) of that statistic [*Barabasi and Stanley*, 1995]. The interface width identifies dominant roughness and the saturation length is a measure of the range of wavelength populations. The standard deviation within each moving window can also be calculated for the same surfaces where the peak value identifies the maximum roughness variability for each surface. Moving window analyses can be used to identify convergent values of standard deviation of elevations, maximum height (within each moving window), and root-mean-squared height, RMSH (equation (6)), which are commonly calculated metrics in soil surface roughness studies [*Eitel et al*., 2011; *Haubrock et al*., 2009; *Nield et al*., 2011; *Sankey et al*., 2011].

$$\mathrm{RMSH} = \sqrt{\frac{\sum_{i=1}^{n} (z_i - \mu)^2}{n-1}} \tag{6}$$

where z_i is the height within each grid cell included in the moving window, μ is the mean elevation within the moving window, and n is the number of grid cells within the moving window.

[11] Fourier transform and wavelet analyses can be used to determine dominant wavelengths of surface topography [*Harrison and Lo*, 1996] and, following the methods of *Perron et al*. [2008] and *Booth et al*. [2009], have been used to identify landscape roughness variation (e.g., sea floor ripples [*Lyons et al*., 2002] and glacial ice [*Nield et al*., 2013]). Fourier transforms are advantageous over single transect methods as they identify the strength of spatial relationships for different spacing and can determine multiple wavelength dominance. Wavelet analysis is similar to Fourier transform analysis, but it calculates spectra locally and so it is able to identify trends on spatially heterogeneous surfaces. Mexican Hat wavelets are typically used as they replicate the roughness element shape [*Booth et al*., 2009]. Pattern variations can be identified by normalizing both Fourier transform and wavelet spectra using spectra from measurements of a smooth surface.

[12] The actual area of a continuous spatial surface can be calculated following the methods of *Jenness* [2004], thereby enabling an areal roughness density to be calculated (equation (7)). It is also possible to quantify the roughness density volumetrically (λ_{vol}) within a unit volume (equation (8)) in a similar way to the volumetric porosity methods of *Grant and Nickling* [1998].

$$R_{\mathrm{SA}} = \frac{\mathrm{SA}_{\mathrm{ridge}}}{\mathrm{SA}_{\mathrm{box}}} \tag{7}$$

$$\lambda_{\mathrm{vol}} = \frac{V_{\mathrm{ridge}}}{V_{\mathrm{box}}} \tag{8}$$

Table 3. Wind Data for Each Site Ordered by z_o Magnitude

Variability Clusters	Height Clusters	Rank (z_o)	Mean Values			Confidence Limits		Standard Deviations		Number of Observations
			z_o (m)	u_* (m/s)	R^2	z_o	u_*	z_o (m)	u_* (m/s)	
A10	H4	1	0.00007	0.248	0.996	0.00017	0.026	0.00006	0.081	5934
A11	H2	2	0.00046	0.218	0.990	0.00154	0.039	0.00030	0.031	195
A8	H4	3	0.00059	0.297	0.997	0.00113	0.030	0.00049	0.086	6745
D1	H2	4	0.00062	0.317	0.995	0.00141	0.038	0.00036	0.097	2124
A4	H2	5	0.00065	0.262	0.992	0.00199	0.043	0.00042	0.052	1416
A12	H2	6	0.00071	0.274	0.992	0.00213	0.045	0.00051	0.053	894
D2	H2	7	0.00126	0.296	0.991	0.00349	0.049	0.00070	0.059	1090
A5	H2	8	0.00237	0.345	0.996	0.00386	0.037	0.00119	0.099	2534
A9	H2	9	0.00250	0.351	0.996	0.00439	0.039	0.00128	0.110	2968
A6	H1	11	0.00263	0.379	0.996	0.00462	0.043	0.00118	0.104	2093
A7	H2	12	0.00263	0.344	0.996	0.00424	0.036	0.00158	0.080	2650
A2	H1	10	0.00270	0.374	0.993	0.00559	0.052	0.00110	0.078	3292
B2	H1	13	0.00297	0.375	0.994	0.00587	0.049	0.00124	0.073	2934
C2	H1	14	0.00327	0.389	0.995	0.00597	0.047	0.00131	0.086	3469
A3	H1	15	0.00357	0.311	0.995	0.00671	0.040	0.00184	0.057	638
A1	H1	16	0.00500	0.432	0.991	0.01109	0.075	0.00598	0.141	1104
B1	H1	17	0.00598	0.389	0.992	0.01199	0.059	0.00186	0.059	671
C1	H5	18	0.00723	0.407	0.993	0.01420	0.062	0.00279	0.067	782
B3	H3	19	0.00793	0.193	0.988	0.00757	0.038	0.00333	0.050	54
B4	H6	20	0.00963	0.346	0.987	0.00980	0.072	0.00376	0.038	22

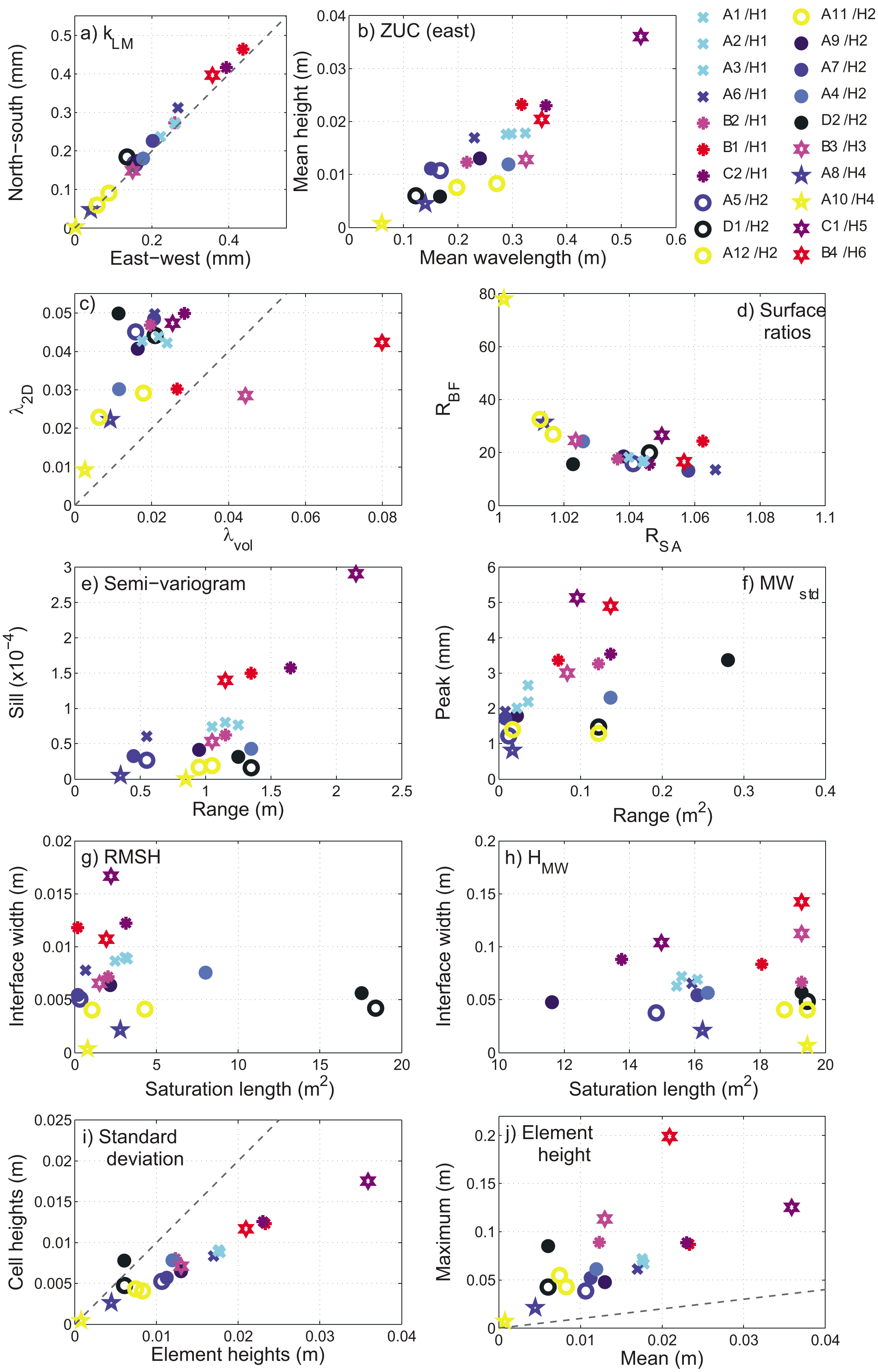

Figure 2. (a–j) Relationships between key surface morphology metrics. Data points represent each of the 20 surfaces and are colored by assigned variability cluster groups (see Figure 4 for membership), and symbols indicate height cluster groups (see Figure 5 for membership), as indicated by the legend labels where A–D indicate variability membership and H1–H6 indicate height membership.

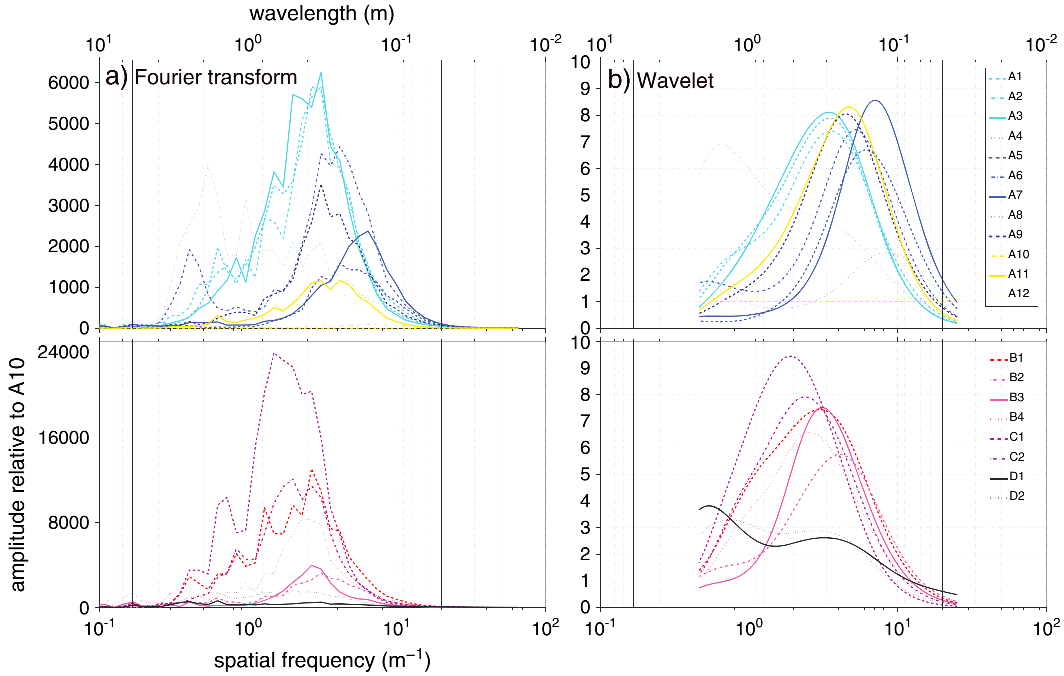

Figure 3. (a) Fourier transform and (b) wavelet spectra arranged and colored using variability cluster groups (Figure 4; legend indicates group labels A–D). Magnitudes of each surface signal have been normalized using the spectra from the flat surface (A10).

where R_{SA} is the areal roughness density based on surface area, SA_{ridge} is the actual surface area of each site, SA_{box} is the planform area of the site, V_{ridge} is the element volume above a plane intersecting the lowest surface point, and V_{box} is the volume of air within which the elements reside, 1 m above the lowest surface point.

[13] We assimilate all of the above methods to classify TLS-measured surface element configurations both in magnitude, shape, and variability using cluster analysis and then determine multiple linear regression relationships between surface metrics and z_o to identify which of these key surface characteristics (magnitude, shape, or variability) has a greater influence on estimating z_o.

3. Study Sites and Field Methods

[14] Twenty surfaces spanning a range of element magnitudes (flat to cobbles) and pattern configurations (regular to irregular) typical of dust-emitting landscapes (Figure 1; Table 2) were measured using a Leica ScanStation TLS in July, August 2011, and August 2012. Eighteen surfaces were located on Sua Pan, part of the Makgadikgadi Salt Pan complex in central Botswana (20.5754°S, 25.959°E). Sua experiences ephemeral surface flooding [*Eckardt et al.*, 2008] and is one of southern Africa's most important aeolian dust source areas [*Bryant et al.*, 2007; *Prospero et al.*, 2002; *Washington et al.*, 2003; *Zender and Kwon*, 2005]. The pan surface comprises a polygon crust (Figures 1a and 1b) of varying morphology and in various states of formation and degradation. The measured surfaces ranged from newly formed, flat crust, to well-formed polygons (Figure 1b). A number of surfaces were degraded with broken and deflated ridges, and some surfaces contained a mix of flat, newly formed crust and extruding and broken crust ridges. Two further surfaces with larger element heights were measured at Kotarjökull and Falljökull sandar in Southeast Iceland (63.925°N, 16.792°W and 63.950°N, 16.832°W, respectively) which are a major source of high-latitude dust [*Prospero et al.*, 2012]. At Kotarjökull we sampled an inactive, stabilized terrace surface with rounded volcanic fluvial deposits. At Falljökull sandur we sampled the active surface, with braided river channels surrounding the measurement site and volcanic fluvial sediments (Figure 1c). Both sandar are flat and exposed to the dominant wind fetch from the south east for several kilometers.

[15] High-resolution surface topography was measured with a specified resolution of 0.005 m at 30 m for the salt crust and 0.01 m at 50 m and 70 m for the Kotarjökull sandur and Falljökull sandur sites, respectively. Upwind of each instrument setup for data analysis, 144 m^2 sections of data were extracted. Data were reduced to a digital elevation model (DEM) of 0.01 m grid resolution, by assigning the average elevation value in each cell to that grid. Mixed pixels were not noticeably influential in point cloud measurements due to the relatively flat surfaces and high incident angle. Replicate scans of the same surface area at two salt pan sites (flat and ridged) during the day indicated mean surface differences less than 0.003 m, which is below the mean error values of 0.0032 to 0.0034 m recorded from modeled and measured Leica TLS data by *Hodge* [2010]. Empty cells were interpolated in Matlab (Mathworks Inc.) using the natural neighbor (continuous convex hull triangulation) method. Occluded areas were limited to the ridge and rock sides facing away from the TLS on the surfaces with taller elements. Analysis undertaken on independent 5 × 5 m squares produced similar metric results, suggesting interpolation of away facing elements did not adversely influence analysis of the larger surface areas. Larger-scale surface gradients on the sandar were removed by subtracting the underlying

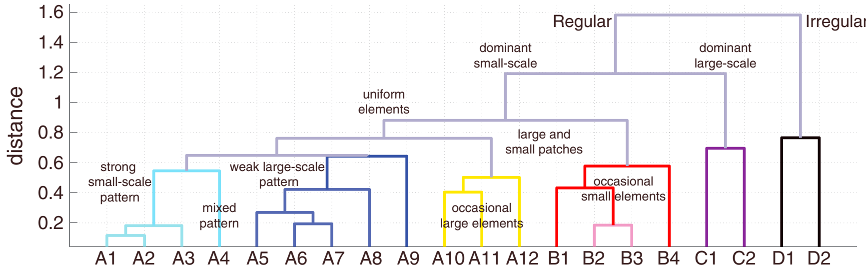

Figure 4. Dendrogram for variability cluster groups (see Table 1 for list of contributing metrics).

surface calculated using a 0.26 m^2 moving window average. Manual measurements of surface bumps using the raw TLS point data along six transects for each sandur following the Gaussian bump fitting methods of *Kean and Smith* [2006a, 2006b] produced similar mean height (difference < 0.001 m) and wavelength (difference < 0.05 m) values as the automated transects on the detrended surfaces.

[16] Wind speeds on Sua Pan were measured at four heights above the surface (at 0.25 m, 0.47 m, 0.89 m, and 1.68 m) with Vector Instruments rotating cup anemometers (A-100R). Analysis was restricted to easterly wind measurements (45° to 135° from north; the dominant storm direction) within a 2-week period centered on the same day as the TLS measurements were collected at each site. At the sandur sites, wind speeds were measured at five heights above the surface (at 0.08 m, 0.48 m, 1.02 m, 1.69 m, and 2.4 m) with RM Young cup anemometers and wind measurements over 4 h periods were analyzed. All wind speed measurements from each site and location were averaged over 1 min to calculate shear velocity (u_*) and aerodynamic roughness values (z_o) following standard law of the wall profile methods [*Oke*, 1987]. Measurements were filtered to minimize any buoyancy effects with a threshold for wind speed at the lowest anemometer height of 3 ms^{-1} and 1 ms^{-1} for the salt pan and sandar, respectively. All instances where the R^2 values for the log-linear regression of height against wind speed to calculate u_* and z_o that were below 0.98 were also discarded [*Bauer et al.*, 1992; *Namikas et al.*, 2003]. Table 3 indicates the number of measurements used for each calculation.

4. Spatial Variability in TLS-Measured Surface Roughness

[17] The 20 measured surfaces covered a range of element heights (0.001–0.036 m mean height and 0.007–0.199 m maximum heights using the zero-up-crossing method), ridge spacing (0.058–0.536 m mean wavelength), and pattern variability (Figure 2). k_{LM} values calculated in wind perpendicular and parallel direction indicate that there was no dominant directional bias within the data (Figure 2a; correlation coefficient = 0.99, $p < 0.001$). The mean wavelengths measured by the zero-up-crossing transect method strongly correlated to the minimum wavelengths found using the Fourier transforms (Figures 2b and 3a; coefficient = 0.82). Wavelet peaks (Figure 3b) indicate the smallest wavelengths identified by the Fourier analysis, and the wavelet peak widths span similar ranges, but the Fourier spectra are more advantageous as they identify individual wavelengths within the data set distribution and so are useful for identifying multiple scales of patterning across the surface.

[18] The 20 surfaces were independently grouped using cluster analysis into two sets to identify surfaces with similar pattern variability (Figure 4) or height characteristics (Figure 5) and to explore the relationships of these pattern types to aerodynamic roughness. The metric sets used for each of the variability and height clusters are defined a priori in Table 1, and planform plots of each surface arranged by pattern variability clusters are shown in Figure 6.

[19] The variability cluster analysis (Figures 4 and 6) identified four main groups (based on greatest dendrogram distance gap). These groups (and subgroups) were qualitatively characterized by independent analysis of the normalized Fourier transform and wavelet spectra (Figure 3). The first dendrogram arm separates regular (A, B and C) from irregular (D) surfaces. Group A is predominantly composed of uniform elements, Group B has occasional larger elements, and Group C consists of dominant larger-scale wavelengths. Within Group A, A1 to A3 have strong small-scale patterns, A5 to A9 have very weak large scale patterns, and A10 to A12 have occasional larger elements. A4 has a mix of patterns, indicated by multiple peaks of similar magnitude on the normalized Fourier transform spectra (Figure 3). Group B has larger elements and spacing

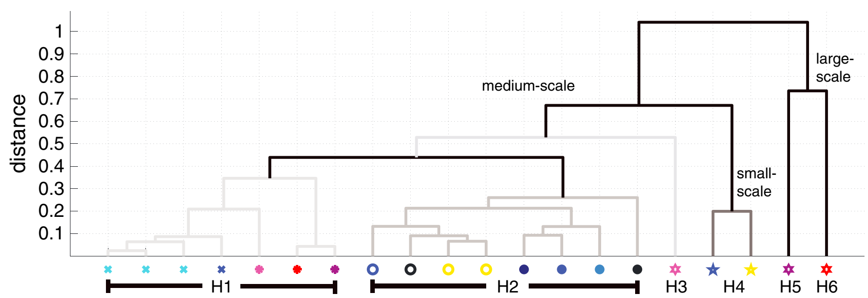

Figure 5. Dendrogram for height cluster groups (see Table 1 for list of contributing metrics). Colors represent variability clusters (Figure 4), and symbols correspond to height clustering.

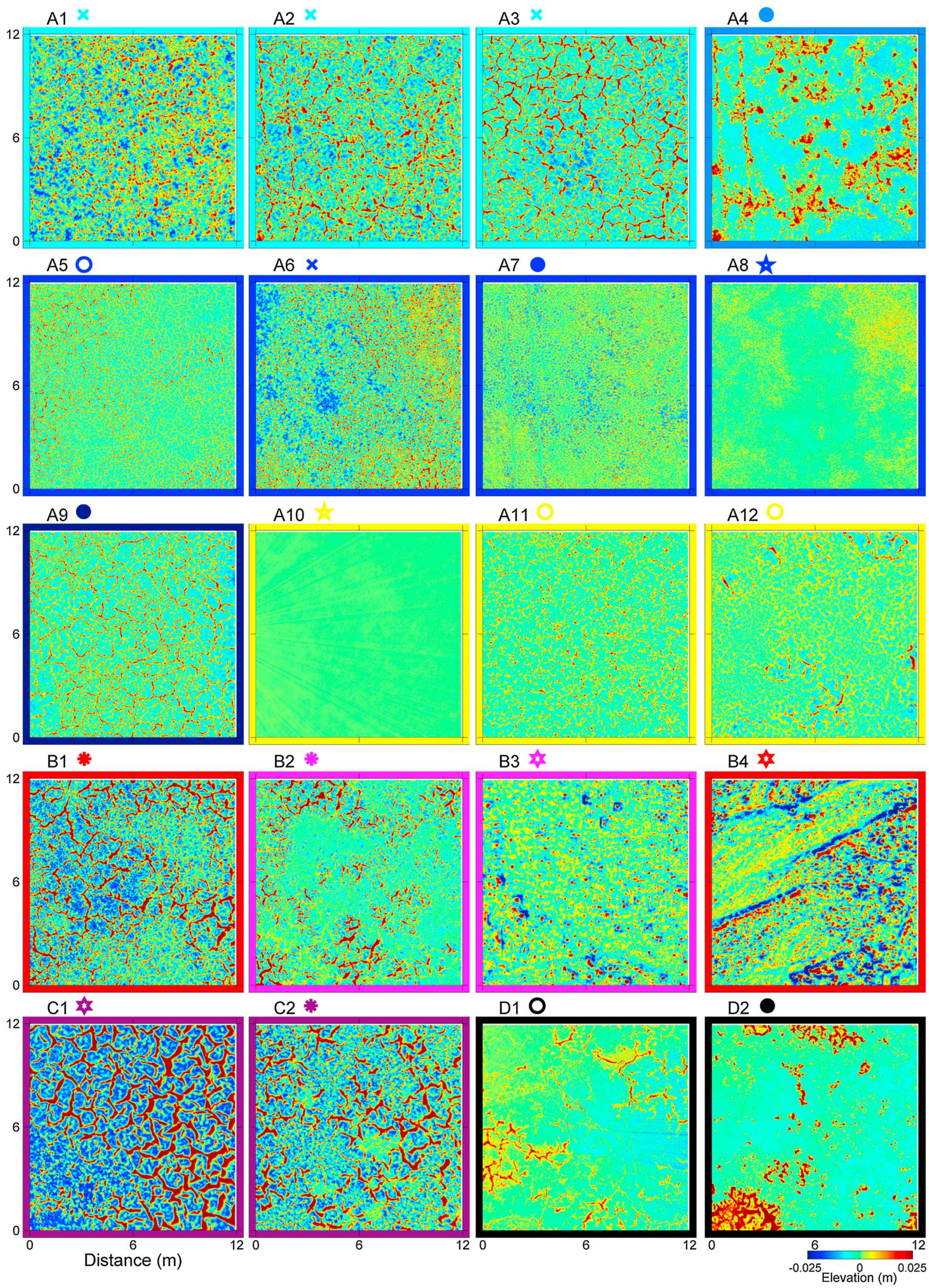

Figure 6. Planform plot of each of the surfaces arranged by variability cluster groups. Colors indicate surface elevation above (red) and below (blue) mean elevation of each surface. Border and symbol colors indicate variability cluster groups (Figure 4), and symbol shapes adjacent to site labels indicate height cluster groups (Figure 5).

Table 4. R^2 Values for Least Square Linear Regression Relationships Between the Natural Logs of Aerodynamic Roughness and the Surface Metrics; Asterisk Indicates p Value Below 0.002[a]

Analysis Dimension	Metric			R^2 All Values	R^2 Excluding Smooth	Model Coefficients Intercept	Model Coefficients Gradient
1-D	Standard deviation of elevation distribution			0.75	0.58	0.65	1.37*
2-D	Zero-up-crossing transects		Height (mean)	0.79	0.65	−0.28	1.33*
			Height (max)	0.75	0.56	−2.02	1.50*
			Height (std)	0.81	0.71	0.29	1.33*
			Ridge width	0.50	0.25	−2.72	1.76*
			Ridge wavelength	0.60	0.38	−3.43	1.89*
			Interridge spacing	0.67	0.50	−1.82	1.89*
			R_{BF}	0.46	0.14	−0.07	−2.03*
			$\lambda_{2\text{-D}}$	0.51	0.19	0.73	2.10*
			k_{LM}	0.76	0.62	1.80	0.92*
	Semivariogram		Sill	0.79	0.67	0.60	0.67*
			Range	0.07	0.08	−6.26	0.73
3-D	Moving window analysis	Mean of elevation standard deviations	Interface width	0.75	0.59	0.47	1.31*
			Saturation length	0.00	0.06	−6.25	−0.04
		Standard deviation of elevation standard deviations	Peak value	0.51	0.51	2.36	1.38*
			Range	0.00	0.00	−5.94	0.05
		Root-mean-squared height (RMSH)	Interface width	0.75	0.59	0.47	1.31*
			Saturation length	0.05	0.18	−6.13	−0.21
		Maximum height	Interface width	0.80	0.67	−1.43	1.66*
			Saturation length	0.09	0.03	0.83	−2.51
	Fourier transform	magnitude relative to flat surface		0.58	0.58	−11.99	0.70*
		dominant wavelength		0.15	0.15	−6.26	−0.35
	Wavelet	magnitude relative to flat surface		0.27	0.27	−8.89	1.49
		dominant wavelength		0.03	0.03	−6.31	−0.21
	R_{SA}			0.53	0.39	−8.13	51.18*
	λ_{vol}			0.79	0.66	−0.01	1.55*
	Height group			0.92	0.87		*
	Shape group			0.86	0.78		*
	Wavelength group			0.81	0.81		*
	Variability group			0.86	0.86		*

[a]Groups refer to sets of metrics identified in Table 1.

generally than Group A, but it also has a mix of larger and smaller scale pattern types, organized in local patches, particularly in the cases of B2 and B3 that have less intense medium scale Fourier transform peaks. Group C is dominated by large-scale elements and wavelengths and has the longest wavelength peaks within the Fourier and wavelet analyses. Group D consists of irregular elements (Figure 1a) with weak relationships between both small and large wavelengths in both the Fourier and wavelet spectra. Visually, Group D consists of large elements in close proximity, isolated from other element assemblages by flat areas, as indicated by the larger saturation length for the RMSH moving window analysis compared to the other surfaces (Figure 2g).

[20] Clustering the surfaces using the height magnitude metrics from Table 1 produced six significant groups (Figure 5). The greatest dendrogram distances separated medium-scale groups (H1, H2, and H3) from small-scale (H4) and large-scale groups (H5 and H6).

[21] A number of metrics are particularly good at distinguishing the different height and variability clusters. Maximum height within moving window separates the variability groups by saturation length and height groups by interface width (Figure 2h). Variability group D has a much larger RMSH saturation length than the rest of the surfaces, but the height of its members (interface width) matches the related height cluster groups (Figure 2g). Aside from the two sandur surfaces (B3/H3 and B4/H6), $\lambda_{2\text{-D}}$ overpredicts roughness density compared to λ_{vol} (Figure 2c). This is because the sandur surfaces do not have the interconnected ridge pattern of the salt pan. For small heights (height cluster group H4), nonspatial and element height standard deviation are similar values, but as pattern magnitude increases (pattern variability group C), the standard deviation of element height increases at a greater rate than the nonspatial value (Figure 2i). Irrespective of pattern cluster group, the members of the largest height clusters (H5 and H6) are end-members for both mean and maximum element height (Figure 2j).

5. Aerodynamic Roughness Variability

[22] Mean and standard deviation values for wind profiles measured at each site from the dominant wind direction are shown in Table 3. Aerodynamic roughness measurements in general followed the height cluster groups (Figure 5) and ranged from 7×10^{-5} m at the smoothest site (A10/H4) to 9.6×10^{-3} m at the roughest site (B4/H6). H3 and H5 groups produced larger z_o values and group H2 generally produced smaller z_o values. Shear velocity measurements ranged from

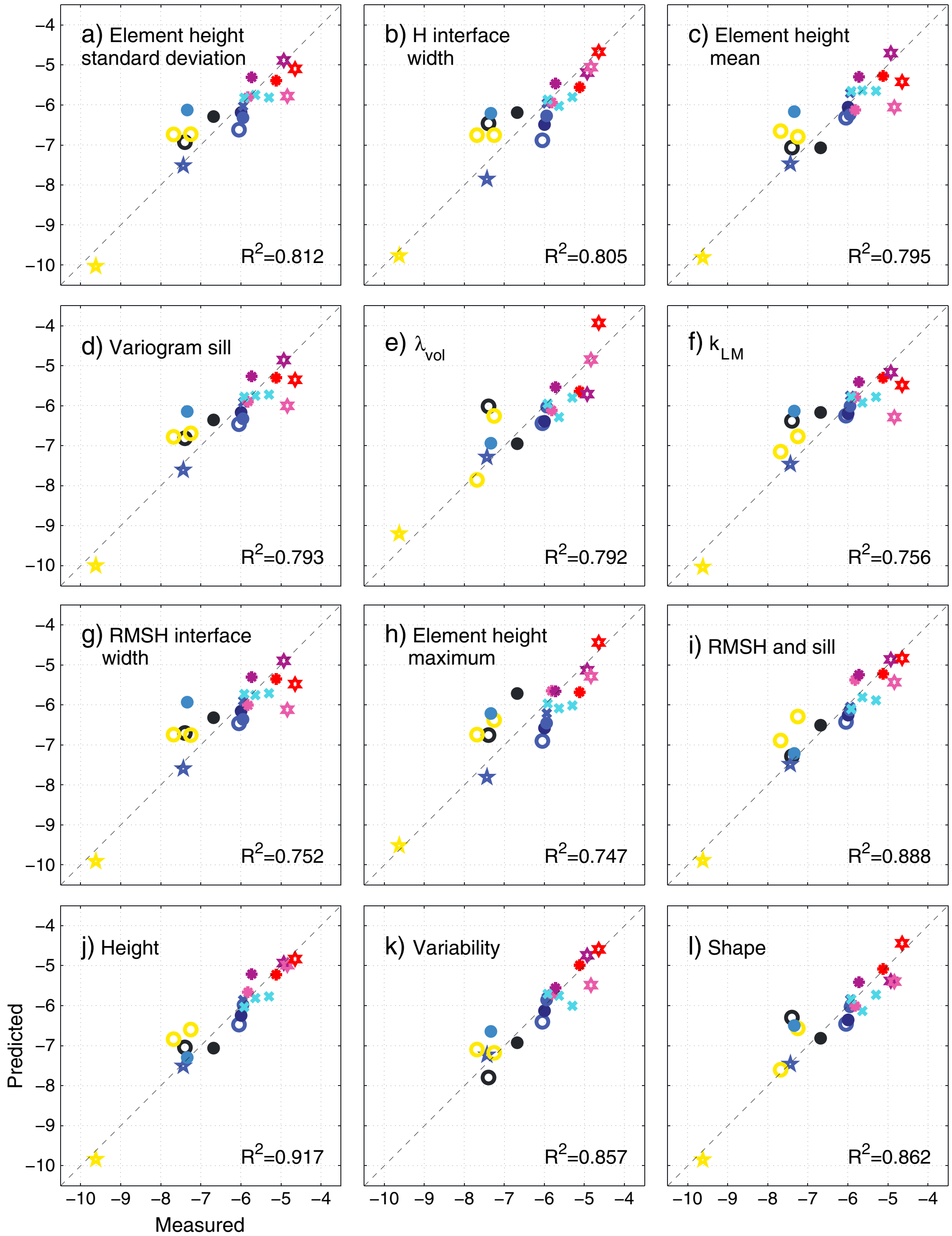

Figure 7. (a–i) Measured and predicted values of the natural log of aerodynamic roughness for the best performing metrics and select groups of metrics (Table 1); $p < 0.001$ for all relationships. Symbol colors indicate variability cluster groups (Figure 4) and symbol shapes adjacent to site labels indicate height cluster groups (Figure 5).

0.19 to 0.43 ms^{-1} and were not related to z_o magnitude ($R^2 = 0.104$). Confidence limits for shear velocities and z_o ranged from 10 to 21% and 95 to 333% of the mean values, respectively.

6. Implications for Quantifying Aerodynamic Roughness of Complex Surfaces

[23] The ability of different surface metrics to characterize aerodynamic roughness is illustrated in Table 4 and Figure 7. In general, variations in aerodynamic roughness (z_o) are controlled more strongly by parameters that include some aspect of surface roughness height in their metrics rather than surface roughness spacing. For example, metrics such as element mean height and standard deviation using the zero-up-crossing method, interface width of maximum height within a moving window, semivariogram sill, and λ_{vol} all have R^2 values greater than 0.79 when regressed against z_o (Figures 7a–7e). Surface roughness descriptors k_{LM}, RMSH interface width, and maximum element height also perform well ($R^2 > 0.74$; Figures 7f–7h). Of these metrics, the standard deviation of element heights, interface width of maximum height within a moving window, and semivariogram sill are less sensitive to the

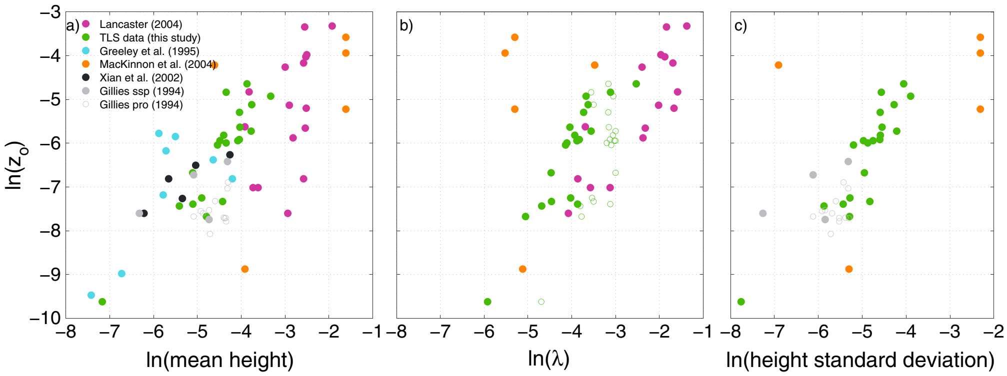

Figure 8. Comparison of (a) mean height, (b) lambda, and (c) standard deviation of element height values from TLS and published data [*Gillies*, 1994; *Greeley et al.*, 1995; *Lancaster*, 2004; *MacKinnon et al.*, 2004; *Xue et al.*, 2002]. The TLS solid green circles are for λ calculated using the 3-D method, hollow circles indicate values calculated using the transect method for an easterly wind.

exclusion of the smooth surface ($R^2 > 0.66$; Table 4). Multiple linear regressions were performed on each of the groups from Table 1 to determine the relationships between shape, height, variability, and wavelength groups (Figures 7j–7l).

$$\ln(z_o) = 0.45\,\text{height} + 0.37\,\text{variability} + 0.20\,\text{shape} + 0.10\,\text{wavelength} + 0.72 \quad \left(R^2 = 0.90; p < 1 \times 10^{-6}\right) \tag{9}$$

$$\ln(z_o) = 0.58\,\text{height} + 0.50\,\text{variability} + 0.48 \quad \left(R^2 = 0.90; p < 1 \times 10^{-7}\right) \tag{10}$$

[24] Coefficients and R^2 values from the multiple linear regressions confirm that height is the most significant of the pattern descriptors with respect to aerodynamic roughness, both for the combination of all metric descriptors (equation (9)) and the combination of height and variability groups only (equation (10)). When a surface consists of larger roughness elements (B3/H3, C1/H5, and B4/H6), the best metric predictors are the interface width of maximum height and element maximum height (Figures 7b and 7h). This agrees with wind tunnel studies that have found maximum height outperforms mean height for nonuniform blocks [*Cheng and Castro*, 2002; *Hagishima et al.*, 2009]. However, these maximum height-based metrics underpredict or overpredict z_o on surfaces with moderate element heights but underlying, weak large-scale pattern variability or irregularity (A4/H2, A11/H2, A12/H2, D1/H2, and D2/H2). Modeling λ_{vol} (Figure 7e) reduces the residual error for some of these surfaces, but has outliers relating to the height groups (D1/H2 and A12/H2), and is less able to predict z_o on some larger surfaces (H5 and H6). The other highly correlated metrics all perform similarly in terms of ability to predict z_o on a uniform surface with small-scale patterns (A1 to A3, A6 to A9, and B1 to B2). Moreover, our results suggest that if surfaces measured at high resolution are quantified using the suite of metrics discussed in this paper, over 90% of the variance can be explained for aerodynamic roughness estimation.

[25] The combination of RMSH and variogram sill (Figure 7i) performs best at reducing pattern specific outliers, but these metrics require detailed surface measurements. More common metrics typically measured using field transects include element height (mean, maximum, and standard deviation) and element width or wavelength (spacing). If we consider only pairs of these commonly measured metrics, where each pair consists of one vertical and one horizontal metric, then irrespective of the exact pairing, multiple linear regressions generate larger coefficients for the height (vertical) component.

$$\ln(z_o) = 1.66\ln(H_{\text{mean}}) - 0.63\ln(W_{\text{mean}}) - 0.08 \quad \left(R^2 = 0.81; p < 1 \times 10^{-6}\right) \tag{12}$$

$$\ln(z_o) = 1.48\ln(H_{\max}) - 0.04\ln(W_{\text{mean}}) - 2.0 \quad \left(R^2 = 0.75; p < 1 \times 10^{-5}\right) \tag{13}$$

[26] where H_{mean} is the mean element height across all transects; $H_{\max}$ is the maximum element height for each transect, averaged across all transects, and W_{mean} is the mean element width.

[27] The inclusion of ridge width or wavelength does not improve the R^2 value from regressions that include only a single height metric by more than 4%. This suggests that in environments where data are limited, an accurate measurement of the mean or maximum element height may be sufficient to explain most of the variance in the aerodynamic roughness height.

[28] Roughness density (λ) is the most common shape descriptor used to relate surface and aerodynamic roughness. Figure 8 compares values of mean height, λ, and standard deviation of height from previous studies of unvegetated surfaces (filtered for appropriate methodologies), and our study, resulting in R^2 values of 0.54, 0.33, and 0.47, respectively ($n = 58, 41, 29$). Some of the variation can be explained by the differences in methodology. *Greeley et al.* [1995] used a laser profiler, but the profile length was 1.2 m along each side of a triangle, so this method is likely to underpredict the presence of large roughness elements, as is evident by the larger residuals for higher z_o values. *Gillies* [1994] used a laser scanner to characterize the surface, but this study was undertaken in a wind tunnel, which may explain the overprediction for very small values of z_o. *MacKinnon et al.* [2004] assumed a cylindrical shape for roughness elements that z_o was measured over and, when this data set is excluded, R^2 values improve to 0.59, 0.69, and 0.74 for mean height, λ,

and standard deviation of height, respectively ($n = 53, 36, 24$). *Lancaster* [2004] only examined elements with a diameter greater than 10 cm, resulting in underprediction of mean element height and λ for small surface roughness and is best modeled using maximum (equation (13)) rather than mean element height (equation (12)). If these points are also excluded, then the R^2 value for mean height increases to 0.65 ($n = 37$). This suggests that if element heights are measured to high precision, mean height performs as well or better than $\lambda_{2\text{-D}}$ for predicting z_o. This agrees with studies of much larger roughness elements that point to the need to include more weighting of element height rather than only roughness density when predicting sediment transport over complex surfaces [*Gillies and Lancaster*, 2013]. While our study has highlighted the importance of height characterization for z_o estimation, further research is needed into sedimentation patterns over these surfaces, and TLS is a useful technique to map these patterns at high resolution.

7. Conclusions

[29] Our findings show that when a surface is measured at high (mm scale) spatial resolution, any metric combination that includes a height-related component will be able to predict aerodynamic roughness (z_o), but the optimal choice depends on the pattern variability of the surface. For surfaces with large elements, or that exhibit mixed homogenous patches of large and small roughness elements, maximum height is the best predictor of z_o while for more uniform surfaces, mean element height or λ_{vol} should be used to predict z_o. Multiple linear regressions indicate that, in general, height is the most significant descriptor, and wavelength is less important for continuous roughness elements found on crusted or rocky surfaces. Where it is possible to measure a complete DEM of surface elevations, a combination of variogram sill and RMSH is the best combination for aerodynamic roughness estimates as this combination is less sensitive to pattern variability. However, our data also suggest that the height of surface roughness provides a good explanation ($R^2 > 0.79$) for most of the variance in aerodynamic roughness (z_o) and performs at least as well as the more complex roughness density metrics. Aerodynamic roughness (z_o) is a fundamental parameter in wind erosion and dust emission modeling, critical in the calculation of shear velocity (u_*) and erosion thresholds. This study is the first to recognize the significance of height for estimating aerodynamic roughness when small-scale complex surface roughness is accurately quantified, irrespective of comparator metric choice. This has very significant implications for the development of aerodynamic roughness predictors which are fundamental to the efficiency of wind erosion models, and, particularly, dust emission schemes in climate models.

[30] **Acknowledgments.** The Botswana fieldwork was partly funded by NERC as part of the DO4models project (NE/H021841/1), with travel support for Nield from a World University Network mobility grant and a University of Southampton SIRDF grant. The Iceland component was funded by a Royal Society Research Grant awarded to Nield (RG090467). Vircavs was supported by the EPSRC Vacation Bursary Scheme (EP/J500537/1 Doctoral Training Account (University of Southampton)). Data processing was undertaken using the IRIDIS High Performance Computing Facility at the University of Southampton. R.T. Wilson is thanked for his assistance with the surface area calculations, J.A. Gillies, A.C.W. Baas, and C.S.B. Grimmond for insightful discussions, and two anonymous reviewers for helpful suggestions.

References

Anderson, K., J. Bennie, and A. Wetherelt (2010), Laser scanning of fine scale pattern along a hydrological gradient in a peatland ecosystem, *Landscape Ecol.*, *25*(3), 477–492.

Antonarakis, A. S., K. S. Richards, J. Brasington, and M. Bithell (2009), Leafless roughness of complex tree morphology using terrestrial lidar, *Water Resour. Res.*, *45*, W10401, doi:10.1029/2008WR007666.

Bauer, B. O., D. J. Sherman, and J. F. Wolcott (1992), Sources of uncertainty in shear-stress and roughness length estimates derived from velocity profiles, *Professional Geogr.*, *44*(4), 453–464.

Blumberg, D. G., and R. Greeley (1993), Field studies of aerodynamic roughness length, *J. Arid Environ.*, *25*, 39–48.

Booth, A. M., J. J. Roering, and J. T. Perron (2009), Automated landslide mapping using spectral analysis and high-resolution topographic data: Puget Sound lowlands, Washington, and Portland Hills, Oregon, *Geomorphology*, *109*(3-4), 132–147.

Brock, B. W., I. C. Willis, and M. J. Shaw (2006), Measurement and parameterization of aerodynamic roughness length variations at Haut Glacier d'Arolla, Switzerland, *J. Glaciol.*, *52*(177), 281–297.

Brown, O. W., and C. H. Hugenholtz (2011), Estimating aerodynamic roughness (z_o) in mixed grassland prairie with airborne LiDAR, *Can. J. Remote Sens.*, *37*(4), 422–428.

Brown, S., W. G. Nickling, and J. A. Gillies (2008), A wind tunnel examination of shear stress partitioning for an assortment of surface roughness distributions, *J. Geophys. Res.*, *113*, F02S06, doi:10.1029/2007JF000790.

Bryant, R. G., G. R. Bigg, N. M. Mahowald, F. D. Eckardt, and S. G. Ross (2007), Dust emission response to climate in southern Africa, *J. Geophys. Res.*, *112*, D09207, doi:10.1029/2005JD007025.

Buckley, S. J., J. A. Howell, H. D. Enge, and T. H. Kurz (2008), Terrestrial laser scanning in geology: Data acquisition, processing and accuracy considerations, *J. Geol. Soc.*, *165*, 625–638.

Bullard, J. E., S. P. Harrison, M. C. Baddock, N. Drake, T. E. Gill, G. McTainsh, and Y. Sun (2011), Preferential dust sources: A geomorphological classification designed for use in global dust-cycle models, *J. Geophys. Res.*, *116*, F04034, doi:10.1029/2011JF002061.

Castro, I. P., H. Cheng, and R. Reynolds (2006), Turbulence over urban-type roughness: Deductions from wind-tunnel measurements, *Boundary Layer Meteorol.*, *118*(1), 109–131.

Cheng, H., and I. P. Castro (2002), Near wall flow over urban-like roughness, *Boundary Layer Meteorol.*, *104*(2), 229–259.

Cheng, H., P. Hayden, A. G. Robins, and I. P. Castro (2007), Flow over cube arrays of different packing densities, *J. Wind Eng. Ind. Aerodynamics*, *95*(8), 715–740.

Croft, H., K. Anderson, and N. J. Kuhn (2012), Reflectance anisotropy for measuring soil surface roughness of multiple soil types, *CATENA*, *93*, 87–96.

Croft, H., K. Anderson, R. E. Brazier, and N. J. Kuhn (2013), Modelling fine scale soil surface structure using geostatistics, *Water Resour. Res.*, *49*, 1858–1870, doi:10.1002/wrcr.20172.

Darmenova, K., I. N. Sokolik, Y. Shao, B. Marticorena, and G. Bergametti (2009), Development of a physically based dust emission module within the Weather Research and Forecasting (WRF) model: Assessment of dust emission parameterizations and input parameters for source regions in Central and East Asia, *J. Geophys. Res.*, *114*, D14201, doi:10.1029/2008JD011236.

Eamer, J. B. R., and I. J. Walker (2010), Quantifying sand storage capacity of large woody debris on beaches using LiDAR, *Geomorphology*, *118*, 33–47.

Eckardt, F. D., R. G. Bryant, G. McCulloch, B. Spiro, and W. W. Wood (2008), The hydrochemistry of a semi-arid pan basin case study: Sua Pan, Makgadikgadi, Botswana, *Appl. Geochem.*, *23*(6), 1563–1580.

Eitel, J. U. H., C. J. Williams, L. A. Vierling, O. Z. Al-Hamdan, and F. B. Pierson (2011), Suitability of terrestrial laser scanning for studying surface roughness effects on concentrated flow erosion processes in rangelands, *CATENA*, *87*(3), 398–407.

Fardin, N., Q. Feng, and O. Stephansson (2004), Application of a new in situ 3D laser scanner to study the scale effect on the rock joint surface roughness, *Int. J. Rock Mech. Mining Sci.*, *41*(2), 329–335.

Frankel, K. L., and J. F. Dolan (2007), Characterizing arid region alluvial fan surface roughness with airborne laser swath mapping digital topographic data, *J. Geophys. Res.*, *112*, F02025, doi:10.1029/2006JF000644.

Gillies, J. A. (1994), A wind tunnel study of the relationships between complex surface roughness form, flow geometry and shearing stress, PhD thesis, Department of Geography, University of Guelph.

Gillies, J. A., W. G. Nickling, and J. King (2007), Shear stress partitioning in large patches of roughness in the atmospheric inertial sublayer, *Boundary Layer Meteorol.*, *122*(2), 367–396.

Gillies, J. A., and N. Lancaster (2013), Large roughness element effects on sand transport, Oceano Dunes, California, *Earth Surf. Processes Landforms*, *38*(8), 785–792.

Glenn, N. F., D. R. Streutker, D. J. Chadwick, G. D. Thackray, and S. J. Dorsch (2006), Analysis of LiDAR-derived topographic information for characterizing and differentiating landslide morphology and activity, *Geomorphology*, *73*(1-2), 131–148.

Goda, Y. (2000), *Random Seas and Design of Maritime Structures*, World Scientific, Singapore.

Grant, P. F., and W. G. Nickling (1998), Direct field measurement of wind drag on vegetation for application to windbreak design and modelling, *Land Degradation Dev.*, *9*(1), 57–66.

Greeley, R., D. G. Blumberg, A. R. Dobrovolskis, L. R. Gaddis, J. D. Iversen, N. Lancaster, K. R. Rasmussen, R. S. Saunders, S. D. Wall, and B. R. White (1995), Potential transport of windblown sand: Influence of surface roughness and assessment with radar data, in *Desert Aeolian Processes*, edited by V. P. Tchakerian, pp. 75–99, Chapman and Hall, New York.

Greeley, R., D. G. Blumberg, J. F. Mchone, A. Dobrovolskis, J. D. Iversen, N. Lancaster, K. R. Rasmussen, S. D. Wall, and B. R. White (1997), Applications of spaceborne radar laboratory data to the study of aeolian processes, *J. Geophys. Res.*, *102*(E5), 10,971–10,983.

Grimmond, C. S. B., and T. R. Oke (1999), Aerodynamic properties of urban areas derived, from analysis of surface form, *J. Appl. Meteorol.*, *38*(9), 1262–1292.

Hagishima, A., J. Tanimoto, K. Nagayama, and S. Meno (2009), Aerodynamic parameters of regular arrays of rectangular blocks with various geometries, *Boundary Layer Meteorol.*, *132*(2), 315–337.

Harrison, J. M., and C. P. Lo (1996), PC-based two-dimensional discrete Fourier transform programs for terrain analysis, *Comp. Geosci.*, *22*(4), 419–424.

Haubrock, S. N., M. Kuhnert, S. Chabrillat, A. Guntner, and H. Kaufmann (2009), Spatiotemporal variations of soil surface roughness from in-situ laser scanning, *CATENA*, *79*(2), 128–139.

Hodge, R. A. (2010), Using simulated Terrestrial Laser Scanning to analyse errors in high-resolution scan data of irregular surfaces, *ISPRS J. Photogramm. Remote Sens.*, *65*(2), 227–240.

Hodge, R., J. Brasington, and K. S. Richards (2009), Analysing laser-scanned digital terrain models of gravel bed surfaces: Linking morphology to sediment transport processes and hydraulics, *Sedimentology*, *56*(7), 2024–2043.

Huang, G. H., and C. K. Wang (2012), Multiscale geostatistical estimation of gravel-bed roughness from Terrestrial and Airborne Laser Scanning, *Geosci. Remote Sens. Lett. IEEE*, *9*(6), 1084–1088.

Hugenholtz, C. H., O. W. Brown, and T. E. Barchyn (2013), Estimating aerodynamic roughness (z_0) from terrestrial laser scanning point cloud data over un-vegetated surfaces, *Aeolian Res.*, *10*, 161–169.

Jenness, J. S. (2004), Calculating landscape surface area from digital elevation models, *Wildlife Soc. Bull.*, *32*(3), 829–839.

Kaasalainen, S., H. Kaartinen, A. Kukko, K. Anttila, and A. Krooks (2011), Application of mobile laser scanning in snow cover profiling, *Cryosphere*, *5*(1), 135–138.

Kean, J. W., and J. D. Smith (2006a), Form drag in rivers due to small-scale natural topographic features: 1. Regular sequences, *J. Geophys. Res.*, *111*, F04009, doi:10.1029/2006JF000467.

Kean, J. W., and J. D. Smith (2006b), Form drag in rivers due to small-scale natural topographic features: 2. Irregular sequences, *J. Geophys. Res.*, *111*, F04010, doi:10.1029/2006JF000490.

Khoshelham, K., D. Altundag, D. Ngan-Tillard, and M. Menenti (2011), Influence of range measurement noise on roughness characterization of rock surfaces using terrestrial laser scanning, *Int. J. Rock Mech. Mining Sci.*, *48*(8), 1215–1223.

King, J., W. G. Nickling, and J. A. Gillies (2006), Aeolian shear stress ratio measurements within mesquite-dominated landscapes of the Chihuahuan Desert, New Mexico, USA, *Geomorphology*, *82*(3-4), 229–244.

King, J., W. G. Nickling, and J. A. Gillies (2008), Investigations of the law-of-the-wall over sparse roughness elements, *J. Geophys. Res.*, *113*, F02S07, doi:10.1029/2007JF000804.

Lancaster, N. (2004), Relations between aerodynamic and surface roughness in a hyper-arid cold desert: Mcmurdo Dry Valleys, Antarctica, *Earth Surf. Processes Landforms*, *29*(7), 853–867.

Lancaster, N., and A. Baas (1998), Influence of vegetation cover on sand transport by wind: Field studies at Owens Lake, California, *Earth Surf. Processes Landforms*, *23*(1), 69–82.

Lancaster, N., W. G. Nickling, and J. A. Gillies (2010), Sand transport by wind on complex surfaces: Field studies in the McMurdo Dry Valleys, Antarctica, *J. Geophys. Res.*, *115*, F03027, doi:10.1029/2009JF001408.

Laurent, B., B. Marticorena, G. Bergametti, P. Chazette, F. Maignan, and C. Schmechtig (2005), Simulation of the mineral dust emission frequencies from desert areas of China and Mongolia using an aerodynamic roughness length map derived from the POLDER/ADEOS 1 surface products, *J. Geophys. Res.*, *110*, D18S04, doi:10.1029/2004JD005013.

Lettau, H. (1969), Note on aerodynamic roughness-parameter estimation on the basis of roughness-element description, pp. 828–832.

Lyles, L., and B. E. Allison (1979), Wind profile parameters and turbulence intensity over several roughness element geometries, *Trans.Asae*, *22*(2), 334–343.

Lyons, A. P., W. L. J. Fox, T. Hasiotis, and E. Pouliquen (2002), Characterization of the two-dimensional roughness of wave-rippled sea floors using digital photogrammetry, *Oceanic Eng. IEEE J.*, *27*(3), 515–524.

MacKinnon, D. J., G. D. Clow, R. K. Tigges, R. L. Reynolds, and P. S. Chavez (2004), Comparison of aerodynamically and model-derived roughness lengths (z(o)) over diverse surfaces, central Mojave Desert, California, USA, *Geomorphology*, *63*(1-2), 103–113.

Mahowald, N. M., R. G. Bryant, J. del Corral, and L. Steinberger (2003), Ephemeral lakes and desert dust sources, *Geophys. Res. Lett.*, *30*(2), 1074, doi:10.1029/2002GL016041.

Manes, C., M. Guala, H. Löwe, S. Bartlett, L. Egli, and M. Lehning (2008), Statistical properties of fresh snow roughness, *Water Resour. Res.*, *44*, W11407, doi:10.1029/2007WR006689.

Marticorena, B., and G. Bergametti (1995), Modeling the atmospheric dust cycle: 1. Design of a soil-derived dust emission scheme, *J. Geophys. Res.*, *100*(D8), 16,415–16,430.

Marticorena, B., et al. (2006), Surface and aerodynamic roughness in arid and semiarid areas and their relation to radar backscatter coefficient, *J. Geophys. Res.*, *111*, F03017, doi:10.1029/2006JF000462.

Millward-Hopkins, J. T., A. S. Tomlin, L. Ma, D. Ingham, and M. Pourkashanian (2011), Estimating aerodynamic parameters of urban-like surfaces with heterogeneous building heights, *Boundary Layer Meteorol.*, *141*(3), 443–465.

Munro, D. S. (1989), Surface-roughness and bulk heat-transfer on a glacier - Comparison with eddy-correlation, *J. Glaciol.*, *35*(121), 343–348.

Nakayama, H., T. Takemi, and H. Nagai (2011), LES analysis of the aerodynamic surface properties for turbulent flows over building arrays with various geometries, *J. Appl. Meteorol. Climatol.*, *50*(8), 1692–1712.

Namikas, S. L., B. O. Bauer, and D. J. Sherman (2003), Influence of averaging interval on shear velocity estimates for aeolian transport modeling, *Geomorphology*, *53*(3-4), 235–246.

Nield, J. M., and G. F. S. Wiggs (2011), The application of terrestrial laser scanning to aeolian saltation cloud measurement and its response to changing surface moisture, *Earth Surf. Processes Landforms*, *36*(2), 273–278.

Nield, J. M., G. F. S. Wiggs, and R. S. Squirrell (2011), Aeolian sand strip mobility and protodune development on a drying beach: Examining surface moisture and surface roughness patterns measured by terrestrial laser scanning, *Earth Surf. Processes Landforms*, *36*(4), 513–522.

Nield, J. M., R. C. Chiverrell, S. E. Darby, J. Leyland, L. H. Vircavs, and B. Jacobs (2013), Complex spatial feedbacks of tephra redistribution, ice melt and surface roughness modulate ablation on tephra covered glaciers, *Earth Surf. Processes Landforms*, *38*, 94–102.

Oke, T. R. (1987), *Boundary Layer Climates*, Routledge, London.

Paul-Limoges, E., A. Christen, N. C. Coops, T. A. Black, and J. A. Trofymow (2013), Estimation of aerodynamic roughness of a harvested Douglas-fir forest using airborne LiDAR, *Remote Sens. Environ.*, *136*, 225–233.

Perron, J. T., J. W. Kirchner, and W. E. Dietrich (2008), Spectral signatures of characteristic spatial scales and nonfractal structure in landscapes, *J. Geophys. Res.*, *113*, F04003, doi:10.1029/2007JF000866.

Prigent, C., I. Tegen, F. Aires, B. Marticorena, and M. Zribi (2005), Estimation of the aerodynamic roughness length in arid and semi-arid regions over the globe with the ERS scatterometer, *J. Geophys. Res.*, *110*, D09205, doi:10.1029/2004JD005370.

Prospero, J. M., P. Ginoux, O. Torres, S. E. Nicholson, and T. E. Gill (2002), Environmental characterization of global sources of atmospheric soil dust identified with the Nimbus 7 Total Ozone Mapping Spectrometer (TOMS) absorbing aerosol product, *Rev. Geophys.*, *40*(1), 1002, doi:10.1029/2000RG000095.

Prospero, J. M., J. E. Bullard, and R. Hodgkins (2012), High-latitude dust over the North Atlantic: Inputs from Icelandic proglacial dust storms, *Science*, *335*(6072), 1078–1082.

Raupach, M. R. (1992), Drag and drag partition on rough surfaces, *Boundary Layer Meteorol.*, *60*(4), 375–395.

Raupach, M. R., R. A. Antonia, and S. Rajagopalan (1991), Rough-wall turbulent boundary layers, *Appl. Mech. Rev.*, *44*(1), 1–25.

Raupach, M. R., D. A. Gillette, and J. F. Leys (1993), The effect of roughness elements on wind erosion threshold, *J. Geophys. Res.*, *98*(D2), 3023–3029.

Rodriguez-Caballero, E., Y. Canton, S. Chamizo, A. Afana, and A. Sole-Benet (2012), Effects of biological soil crusts on surface roughness and implications for runoff and erosion, *Geomorphology*, *145*, 81–89.

Rotach, M. W. (1995), Profiles of turbulence statistics in and above an urban street canyon, *Atmos. Environ.*, *29*(13), 1473–1486.

Sankey, J. B., N. F. Glenn, M. J. Germino, A. I. N. Gironella, and G. D. Thackray (2010), Relationships of aeolian erosion and deposition with LiDAR-derived landscape surface roughness following wildfire, *Geomorphology*, *119*(1-2), 135–145.

Sankey, J. B., J. U. H. Eitel, N. F. Glenn, M. J. Germino, and L. A. Vierling (2011), Quantifying relationships of burning, roughness, and potential dust emission with laser altimetry of soil surfaces at submeter scales, *Geomorphology*, *135*(1-2), 181–190.

Sankey, J. B., S. Ravi, C. S. A. Wallace, R. H. Webb, and T. E. Huxman (2012), Quantifying soil surface change in degraded drylands: Shrub encroachment and effects of fire and vegetation removal in a desert grassland, *J. Geophys. Res.*, *117*, G02025, doi:10.1029/2012JG002002.

Schirmer, M., and M. Lehning (2011), Persistence in intra-annual snow depth distribution: 2. Fractal analysis of snow depth development, *Water Resour. Res.*, *47*, W09517, doi:10.1029/2010WR009429.

Shaw, P. A., and R. G. Bryant (2011), Pans, playas and salt lakes, in *Arid Zone Geomorphology*, pp. 373–401, John Wiley, Ltd., Chichester, West Sussex, U. K.

Smith, M. W., N. J. Cox, and L. J. Bracken (2011), Terrestrial laser scanning soil surfaces: A field methodology to examine soil surface roughness and overland flow hydraulics, *Hydrol. Processes*, *25*(6), 842–860.

Washington, R., M. Todd, N. J. Middleton, and A. S. Goudie (2003), Dust-storm source areas determined by the total ozone monitoring spectrometer and surface observations, *Ann. Assoc. Am. Geogr.*, *93*(2), 297–313.

Weligepolage, K., A. S. M. Gieske, and Z. Su (2012), Surface roughness analysis of a conifer forest canopy with airborne and terrestrial laser scanning techniques, *Int. J. Appl. Earth Observation Geoinformation*, *14*(1), 192–203.

Wiggs, G., and P. Holmes (2011), Dynamic controls on wind erosion and dust generation on west-central Free State agricultural land, South Africa, *Earth Surf. Processes Landforms*, *36*(6), 827–838.

Wirz, V., M. Schirmer, S. Gruber, and M. Lehning (2011), Spatio-temporal measurements and analysis of snow depth in a rock face, *Cryosphere*, *5*(4), 893–905.

Wolfe, S. A., and W. G. Nickling (1993), The protective role of sparse vegetation in wind erosion, *Prog. Phys. Geogr.*, *17*(1), 50–68.

Xue, X., T. Wang, Q. W. Sun, and W. M. Zhang (2002), Field and wind-tunnel studies of aerodynamic roughness length, *Boundary Layer Meteorol.*, *104*(1), 151–163.

Zaki, S. A., A. Hagishima, J. Tanimoto, and N. Ikegaya (2011), Aerodynamic parameters of urban building arrays with random geometries, *Boundary Layer Meteorol.*, *138*(1), 99–120.

Zender, C. S., and E. Y. Kwon (2005), Regional contrasts in dust emission responses to climate, *J. Geophys. Res.*, *110*, D13201, doi:10.1029/2004JD005501.